Classification of Hematologic Malignancies using Texton Signatures

Oncel Tuzel[1], Lin Yang[2,3], Peter Meer[1,2], David J. Foran[3]

[1] Department of Computer Science
   Rutgers University
   Piscataway, NJ 08854, USA

[2] Department of Electrical & Computer Engineering
   Rutgers University
   Piscataway, NJ 08854, USA

[3] Center for Biomedical Imaging & Informatics
   University of Medicine & Dentistry of New Jersey
   Piscataway, NJ 08854, USA

Abstract We describe a decision support system to distinguish among hematology cases directly from microscopic specimens. The system uses an image database containing digitized specimens from normal and four different hematologic malignancies. Initially, the nuclei and cytoplasmic components of the specimens are segmented using a robust color gradient vector flow active contour model. Using a few cell images from each class, the basic texture elements (textons) for the nuclei and cytoplasm are learned, and the cells are represented through texton histograms. We propose to use support vector machines on the texton histogram based cell representation and achieve major improvement over the commonly used classification methods in texture research. Experiments with 3691 cell images from 105 patients which originated from four different hospitals indicate more than 84% classification performance for individual cells and 89% for case based classification for the five class problem.

1 Introduction

Over the past few years there has been increased interest and efforts applied to utilizing content-based image retrieval in medical applications [18, 24, 25, 28, 29, 41]. Individual strategies and approaches differ according to the degree of generality (general purpose versus domain specific), the level of feature abstraction (primitive features versus logical features), overall dissimilarity measure used in retrieval ranking, database indexing procedure, level of user intervention (with or without relevance feedback), and by the methods used to evaluate their performance. In this paper, we present a decision system utilizing texture based representation and support vector machine (SVM) optimization to classify hematologic malignancies.

Send offprint requests to: CAIP Center, 96 Frelinghuysen Road, Piscataway, NJ, 08854

The use of texture analysis for performing automated classification of disease based on features extracted from radiological imaging studies has been reported in the medical literature repeatedly. It has been successfully applied in breast cancer [32, 33, 42], liver cancer [23] and obstructive lung disease [2].

Recently there have been a number of investigators who have begun to explore the feasibility of utilizing texture features in the classification of pathology at the microscopic level. The success of the methods vary with the domain of the problem, and the choice of representation and optimization techniques. We also note that the testing methodology that is applied during the experiments and the size of the datasets have very important role in the observed results, and some test methodologies and small datasets can trigger biased results.

In [37], frequency domain features are used to classify among subclasses of normal and abnormal cervical cell images using a database containing 110 cells from both normal and abnormal groups. Using the spectra of cell images, 27 texture features are extracted with gray level difference method and together with 22 frequency components, resulted in 92% correct classification among subclasses. In [46], statistical geometric features, which are computed from several binary thresholded versions of texture images are used to classify among normal and abnormal cervical cells. The method gave 93% correct classification rate on a database containing 117 cervical cells using only 9 statistical features.

A discrimination scheme among the main subsets of lung carcinomas was reported in [40] by chromatin texture feature analysis using a test set comprised of 195 specimens. Texture features describing the granularity and the compactness of the nuclear chromatin were extracted for calculation of classification rules, which allowed the discrimination of different tumor groups. Although the classification failed to distinguish among some subtypes of tumor groups, around 90% classification accuracy was achieved for small-cell and non-small-cell lung carcinoma using the four dimensional texture features combined with simple decision rules.

In [34], adaptive texture features were described utilizing the class distances and differences of gray level cooccurrence matrices of texture images. In [35], the adaptive texture features were used for classifying the nuclei of cells in ovarian cancer. In this study a clear relation between nuclear DNA content, area, first-order statistics, and texture is observed. The approach discriminated the two classes of cancer with a correct classification rate of 70% on a test set of 134 cases.

A decision support system to discriminate among three types of lymphoproliferatie disorders and normal blood cells was presented in [5]. Cells were represented with their nuclear shape, texture and area, where shape was characterized through similarity invariant Fourier descriptors and multiresolution simultaneous autoregressive model was utilized for texture description. The experiments conducted on a database consisting of 261 specimens using ten-fold cross validation were resulted with 80% correct classification rate. Notice that in all the methods described, the results were acquired using small datasets and without obeying the separation of cells among training-testing sets based on patient. We present a detailed discussion about the testing methodologies and their effects on the results in Section 5.

As new treatments emerge, each targeting specific clinical profiles, it becomes increasingly important to distinguish among subclasses of pathologies. In modern diagnostic pathology, sophisticated analyses are often needed to support a differential diagnosis, but these supporting tests are not typically employed unless morphological assessment of a specimen first leads one to classify the case as suspicious. In many cases, the differential diagnosis can only be rendered after immunophenotyping and/or molecular or cytogenetic study of the cells involved. Immunophenotyping is the process commonly used to analyze and sort lymphocytes into subsets based on their antigens using flow cytometry. For the purposes of our experiments the immunophenotype provide independent confirmation of the diagnosis for all cases. The additional studies are expensive, time consuming, and usually require fresh tissue which may not be readily available. Since it is impractical to immunophenotype every sample that is flagged by a complete blood count (CBC) device,
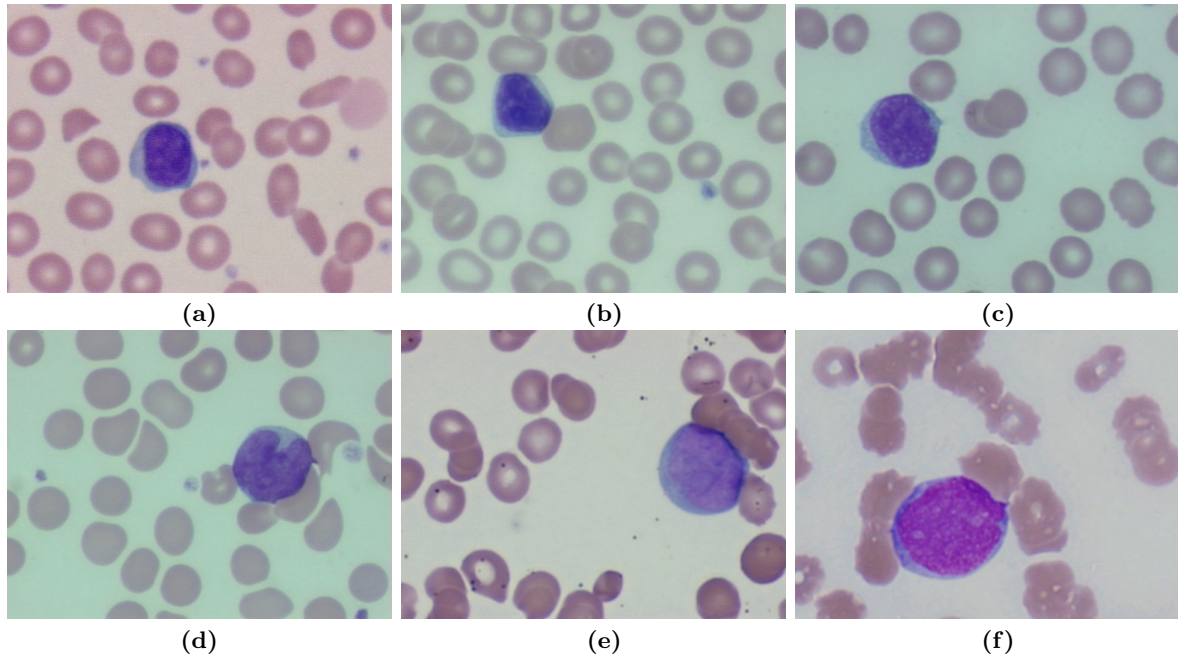
Fig. 1 Representative morphologies for normal and disorders under study. (a) Normal; (b) Chronic Lymphocytic Leukemia - CLL; (c) Mantle Cell Lymphoma - MCL; (d) Follicular Center Cell Lymphoma - FCC; (e) Acute Myeloblastic Leukemia - AML; (f) Acute Lymphoblastic Leukemia - ALL.

passing the specimen through a reliable image-based screening system could potentially reduce cost and patient morbidity.

We designed a texture based solution which distinguishes between normal cells and four different hematologic malignancies. We discriminate among lymphoproliferatie disorders, Chronic Lymphocytic Leukemia (CLL), Mantle Cell Lymphoma, (MCL), Follicular Center Cell Lymphoma (FCC), which can be confused with one another during routine microscopic evaluation. Two acute leukemias, Acute Myelocytic Leukemia (AML) and Acute Lymphocytic Leukemia (ALL), could only be classified in relation to the lymphoproliferatie disorders and normal cells as a single unit labeled as Acute Leukemia. It is shown in [36] that there is no statistical significance in morphometric variables for some subtypes of Acute Leukemia which coincides with our observations. Although each of the disorders under study can exhibit a range of morphological characteristics Figure 1 shows representative morphologies for each.

Chronic Lymphocytic Leukemia (CLL) is the most frequent leukemia in the United States. It is typically a long-term but incurable disease with potential for a more aggressive treatment, e.g. [38]. Mantle Cell Lymphoma (MCL) is a recently described entity (1992) which was not part of the initial working formulation classification system for non-Hodgkin's lymphoma [3]. Timely and accurate diagnosis of MCL is of extreme importance since it has a more aggressive clinical course than CLL or FCC [15,43]. The third lymphoproliferative disorder under study is Follicular Center Cell Lymphoma (FCC), which is a low-grade lymphoma [1].

Chronic leukemias are associated, at least initially, with well-differentiated, or differentiating leukocytes and a relatively slow course. On the other hand, Acute Leukemias are characterized by the presence of very immature cells (blasts) and by the rapidly fatal course in untreated patients. Acute Leukemia primarily affect adults, with the incidence increasing with age. Despite differences in their cell origin, subtypes of Acute Leukemias share important morphological and clinical features [7]. Our database includes two subtypes of

Acute Leukemia, Acute Lymphoblastic Leukemia (ALL) and Acute Myeloblastic Leukemia (AML), but in this study we consider them as a single unit.

The proposed system proceeds in three steps.

1. Segmentation: Our observations indicate that both the nucleus and the cytoplasm of a cell contain valuable information regarding the underlying pathology, therefore we analyze them separately. Given a microscopic specimen, initially the system locates the region which contains the cell and then using a robust color gradient vector flow (GVF) active contour model [49] segments the region into nuclear and cytoplasmic components.
2. Cell representation: Texture information is used to characterize the morphological structure of normal and diseased cells. A few example images from each disorder are used to create the texton library which captures the structure of texture inside each cells nucleus and cytoplasm. The cells are then represented with two texton histograms corresponding to nuclear and cytoplasmic distribution.
3. Classification: We utilize SVMs over the texton histogram based representation to classify the cell images and observe major improvements over the classical histogram based classification methods in the literature such as k-nearest neighbors (kNN).

We conduct four different experiments. In the first experiment, we compare texture features constructed using different methods that were used traditionally in the literature. In the second experiment, we compare the performance of several classification algorithms applied to texture based diagnosis problem. In the third experiment, we show the discriminative power of the proposed cell representation by comparing with several other commonly used features (shape, area) for hematopathological diagnosis. Finally we compare our method with the method of [5] which aims the same problem but has one less disorder class and observe major improvements.

The paper is organized as follows. Image segmentation is briefly reviewed in Section 2. Section 3 presents the texture based cell representation. In Section 4, we present SVM optimization on texton histograms. Section 5 explains the experimental setup, the database of ground truth cases, and the experimental results of different classification methods, features and comparison with previous methods.

2 Image Segmentation

In order to extract features from the cell images, we start with the *image segmentation*. In our application, the region of interest (ROI) containing the object cell, is *automatically* selected for each image [12]. Both the nuclei and the cytoplasm of cells contain valuable distinguishable information for classification. Therefore, the robust color GVF snake [49], which combines L_2E robust estimation and color gradient, is applied for segmenting both the nuclei and the cytoplasm.

A 2D parametric snake [48] is a curve $\mathbf{x}(s) = (x(s), y(s))$ defined via the parameter $s \in [0, 1]$ to minimize an energy function

$$E_{snake} = \int_0^1 \left(\frac{1}{2} \left(\tau \left| \mathbf{x}'(s) \right|^2 + \rho \left| \mathbf{x}''(s) \right|^2 \right) + E_{ext} \left(\mathbf{x}(s) \right) \right) ds \tag{1}$$

where $\mathbf{x}'(s)$ and $\mathbf{x}''(s)$ are the first and second derivatives of the curve with respect to parameter s, and τ and ρ are constants.

According to Helmholtz theorem, the external energy can be replaced with $-\Theta(x, y)$ in (1), where Θ is the GVF in image coordinates. The GVF is computed as a diffusion of the gradient vectors of a gray-level edge map derived from the image. The diffusion version of the gradient vector can enlarge the capture region
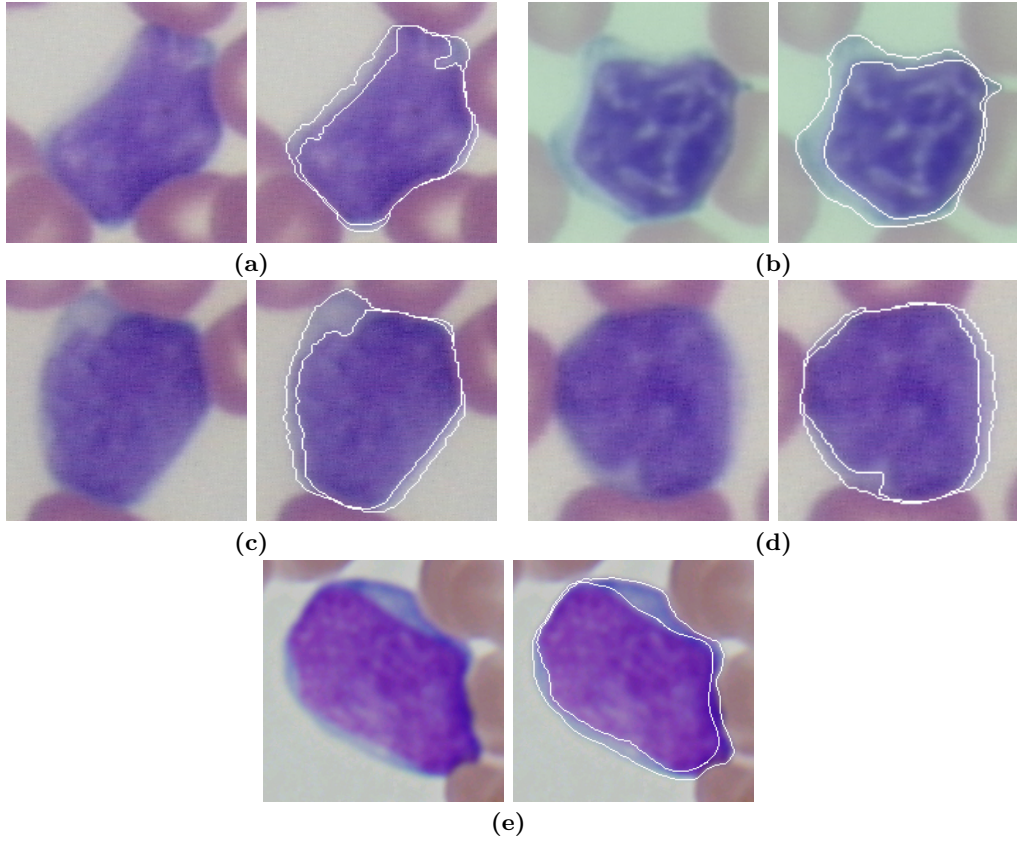
Fig. 2 Image segmentation results applying robust color GVF snake: (a) Normal; (b) CLL; (c) MCL; (d) FCC; (e) Acute Leukemia. The outer and inner curves correspond to cytoplasm and nucleus segmentations respectively.

of tradition snake and also lead the snake into concave regions. It is defined as $\Theta(x, y) = [u(x, y), v(x, y)]$ and minimizes the energy function

$$\Psi = \int \int \left[\eta(u_x^2 + u_y^2 + v_x^2 + v_y^2) + \left(\left| \nabla \left\{ G_{\sigma(x,y)} * I(x, y) \right\} \right|^2 \cdot \left| \Theta(x, y) - \nabla \left\{ G_{\sigma(x,y)} * I(x, y) \right\} \right|^2 \right) \right] dx dy \quad (2)$$

where $\nabla \left\{ G_{\sigma(x,y)} * I(x, y) \right\}$ is the gradient of the input image $I(x, y)$ after Gaussian smoothing with covariance $\sigma^2 I_2$ and mean 0; $u_x ... v_y$ are the partial derivatives w.r.t. x and y; η is a constant. In our approach, the original GVF vector field Θ is replaced by Θ^*, which is the diffusion field in the $L^* u^* v^*$ color space that is more closer to the human perception of color. The color differences in this space can be approximated by Euclidean distances [47, Sect. 3.3.9]. Applying the principle of calculus of variations, the problem is solved by the following Euler-Lagrange differential equation:

$$E_{snake} = \tau \mathbf{x}''(s) - \rho \mathbf{x}''''(s) + \Theta^*(x, y) \quad (3)$$

where $\mathbf{x}''(s)$ and $\mathbf{x}''''(s)$ are the second and fourth derivatives of the curve with respect to the parameter s. Furthermore, instead of randomly choosing initial curves, we apply $L_2 E$ based robust estimation to locate the initial positions, which improves both the convergence speed and the robustness. Figure 2 shows some segmentation results using the approach. The performance of segmentation algorithm slightly varies for different classes of disorders and on average 93% of nuclear and 91% of cytoplasmic components are correctly identified. For more details about the color gradient and robust estimation guided active contour segmentation algorithm, we refer to [49]. Notice that, we convert the images to gray level and normalize

to minimize the effects of imaging conditions *only* after segmentation, since color is an important cue for segmentation.

3 Feature Construction

In this section we describe *texture based* cell representation. A detailed comparison of texture based representation with other common features used in hematapathologic diagnosis is given in Section 5.5.

3.1 Texture Features

The earlier texture research characterizes a texture according to statistical measures of gray level occurrence relation inside the texture image. The most popular methods are gray level difference [16], gray level cooccurrence matrices [17], gray level run length matrices [14] and autoregressive models [31].

In more recent studies, a texture is characterized through textons which are basic repetitive elements of textures. The form of the textons are not known and they are learned through responses to a set of linear filters, and the resulting responses are clustered. The cluster centers are then selected as the textons. The approach has been successfully used in several fields of texture research including classification, segmentation and synthesis [9, 20, 30, 44].

Recently, it has been proposed that the raw pixel values could replace filter responses to characterize a texture. Local intensity information in spatial domain was used for texture synthesis in [11, 21] and texture classification in [45]. In this approach, the neighboring pixels around the pixel of interest are stacked into an array and used as the feature vector.

After filtering the images, each pixel is mapped to d-dimensional space, where d is the number of filters. Similarly, if local neighborhoods are used, d is equal to size of the local neighborhood. A few sample images are selected from each texture class and the filter responses/local neighborhoods are clustered using k-means clustering algorithm [10]. The cluster centers are selected as textons, therefore the k_m parameter of the clustering algorithm determines the number of textons. This process is repeated for all the c texture classes, and the cluster centers are concatenated to each other to form the texton library. There are $c \cdot k_m = p$ textons in the texton library.

The histograms are created by assigning the filter response of each pixel to the closest texton in the texton library (vector quantization) and then finding the occurrence frequencies of each texton throughout the image. The k-means clustering algorithm used during texton library generation finds a suboptimal solution for determining quantization levels in a d-dimensional space, which is enough in many practical situations. Finally, each texture image is modeled via a p-bin texton histogram, representing all classes.

3.2 Cell Representation

The nucleus and cytoplasm of the cells were segmented, as described in Section 2. Following segmentation, the cell images are converted to gray level and *normalized* such that the mean is zero and standard deviation is one. Since the cell images are acquired in different imaging conditions, the normalization is an important operation to minimize the effect of different imaging conditions. The normalization significantly improves the final classification results and supporting claims using similar normalization techniques were also reported
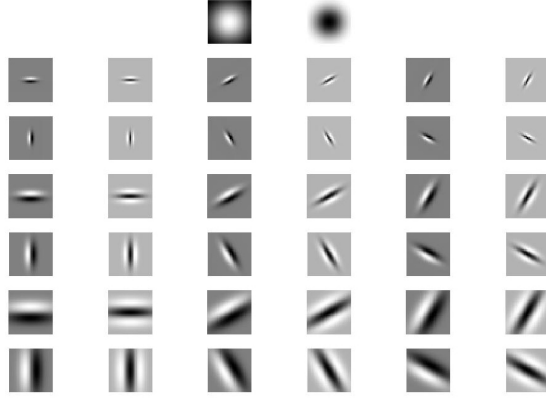
Fig. 3 M8 filter bank. There are total of 38 filters from which two filters are rotationally symmetric (Gaussian and Laplacian of Gaussian) and the remaining 36 filters are edge and bar filters at three different scales.

in [34]. Notice that, the segmentation algorithm described in previous section uses color information, where as texture representation is computed on normalized gray level images.

We compared the performance of classifiers based on different filter banks and local neighborhood in Section 5.3. Although there were not significant differences among some of the filter banks, we found that the **M8** filter bank [44] is the most suitable for our cell representation. The filter bank consists of 38 filters, from which two filters are rotationally symmetric (Gaussian and Laplacian of Gaussian) and 36 of them are edge and bar filters at three scales. We use $\sigma = 10$ for Gaussian and Laplacian of Gaussian functions. The edge and bar filters are selected with $\sigma_x = 1$ and $\sigma_y = 3$ at the finest scale, and are doubled at each of the three scales. The filters are computed at six orientations. Among the oriented filters, only the maximum filter response is retained at each scale, therefore the feature space is $d = 8$ dimensional. The filters in **M8** filter bank are shown in Figure 3. The detailed comparison of different filter banks are explained in Section 5.3.

We analyze the texture of cytoplasm and nucleus independently. A few random cell images ($n_s = 30$) are selected from each class and filter responses inside the segmentation mask are clustered using k-means clustering algorithm with $k_m = 30$. The clustering is performed separately for pixels inside the nucleus and cytoplasm, and repeated for each disease class. Since the size and the variability of cytoplasm texture is less than the nucleus texture, we generate half the number of clusters from the cytoplasm than from the nucleus. We concatenate the cluster centers from each class and construct the texton libraries separately for cytoplasmic and nuclear texture. The algorithm for texton library generation is given in Figure 4.

Using the constructed texton library, the cells are represented with their texton histograms. Given an arbitrary cell image, the pixels inside the cytoplasm and nucleus are filtered and the responses are quantized to the nearest textons in the library. As a result each cell image is represented with two texton histograms of sizes $c \cdot k_m$ and $\frac{c \cdot k_m}{2}$, corresponding to nuclear and cytoplasmic texture. The texton library generation and cell representation process is illustrated in Figure 5.

4 Classification

We utilize *support vector machines* (SVMs) to classify among four types of malignancies and normal cells. SVMs were first introduced in [6] for binary classification problems. The technique is a generalization of linear decision boundaries where decision surface is constructed in a large transformed version of the original feature space.

Input: Cell image samples $\{\mathbf{I}_{j,i}\}$, $i = 1...n_s$ from disease classes $j = 1...c$; cytoplasm and nucleus mask for each cell; number of textons per class k_m.

- Initialize nucleus texton library $\mathbf{T}^N = \emptyset$ and cytoplasm texton library $\mathbf{T}^C = \emptyset$
- **for** $j = 1$ **to** c (for each class)
    - Initialize total filter responses for nucleus $\mathbf{F}^N = \emptyset$ and cytoplasm $\mathbf{F}^C = \emptyset$
    - **for** $i = 1$ **to** n_s (for each sample in the class)
        - Filter image with **M8** filter bank, $\mathbf{F}_{j,i} = \mathbf{f}_{M8} * \mathbf{I}_{j,i}$
        - Concatenate filter responses inside nucleus mask and cytoplasm mask to total responses, $\mathbf{F}^N = [\mathbf{F}^N;\ \mathbf{F}^N_{j,i}]$, $\mathbf{F}^C = [\mathbf{F}^C;\ \mathbf{F}^C_{j,i}]$
    - Cluster filter responses for nucleus and cytoplasm
      $\mathbf{T}^N_j = k\text{-means}(\mathbf{F}^N, k_m)$, $\mathbf{T}^C_j = k\text{-means}(\mathbf{F}^C, k_m/2)$
    - Add cluster centers to texton library
      $\mathbf{T}^N = [\mathbf{T}^N;\ \mathbf{T}^N_j]$, $\mathbf{T}^C = [\mathbf{T}^C;\ \mathbf{T}^C_j]$

Fig. 4 Texton library generation

We first focus on the binary classification problem ($c = 2$). Let $\{(\mathbf{x}_i, y_i)\}_{i=1..n}$ be the training set with the respective class labels, where $\mathbf{x}_i \in \mathbb{R}^p$ and $y_i \in \{\pm 1\}$. The SVM solves the following optimization problem

$$\min_{\boldsymbol{\beta},\beta_0,\xi_i} \left[\frac{1}{2}\boldsymbol{\beta}^T\boldsymbol{\beta} + \gamma \sum_{i=1}^{n} \xi_i \right] \qquad \text{subject to} \qquad y_i(h(\mathbf{x}_i)^T\boldsymbol{\beta} + \beta_0) \geq 1 - \xi_i \quad \xi_i > 0 \qquad i = 1,..,n \qquad (4)$$

where the training samples are mapped to an enlarged space with the function $h(\mathbf{x})$. Minimizing $\boldsymbol{\beta}^T\boldsymbol{\beta}$ is equivalent to maximizing the margin between the positive and negative samples and γ is the tradeoff between the training errors $\{\xi_i\}_{i=1...n}$ and the margin. We maximize the dual problem of (4) since it is a simpler convex quadratic programming problem. The dual problem and the decision function involve mapping $h(\mathbf{x})$ through an inner product, therefore it suffices to define the inner product through a kernel function without defining the mapping. In our implementation we use the linear kernel function, i.e., $K(\mathbf{x}, \mathbf{x}') = \mathbf{x} \cdot \mathbf{x}'$. A more detailed discussion on SVMs can be found in [8].

Next we focus on the multi-class classification problem. The first group of methods construct several binary classifiers and combines them to solve multiclass classification problem. The most popular two methods are *one-against-one* and *one-against-all* classifiers. In one-against-one classifier, a binary classifier is trained for all combinations of classes. Then, the label of a test example is predicted by the majority voting among the classifiers. In one-against-all classifier, for each class a binary classifier is trained by labeling the samples from the class as positive examples and samples from the other classes as negative examples. A query point is assigned to the class having maximum decision function among all the classes.

The second group of methods considers all the classes together and solves the multi-class problem in one step. Due to a large scale optimization problem, these methods are computationally more expensive which makes them unsuitable for large size applications. A detailed comparison of multi-class SVMs can be found in [22].

In this paper we utilize *one-against-one SVM classifier*. Besides we present results for one-against-all SVM classifier, kNN classifier which is widely used for texture classification problems and LogitBoost classifier which allows us to describe the uncertainty of the classification, in Section 5.
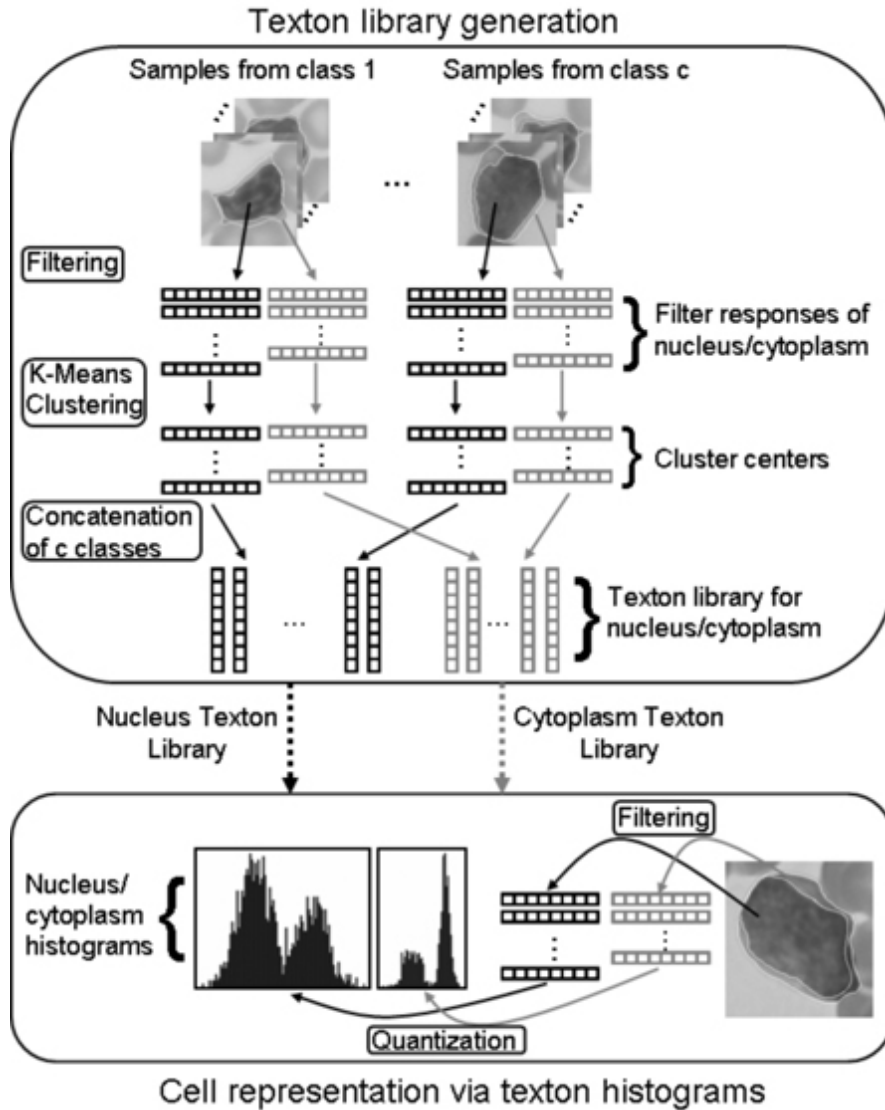
Fig. 5 Texton library generation and cell representation. Black and gray vectors correspond to nuclear and cytoplasmic features respectively.

5 Experiments

5.1 Cell Database

Immunophenotyping was used to confirm the diagnosis for a mixed set of 86 hematopathology cases: 18 Mantle Cell Lymphoma (MCL), 20 Chronic Lymphocytic Leukemia (CLL), 9 Follicular Center Cell lymphoma (FCC), and 39 Acute Leukemia. In addition there were 19 normal cases. For each case, we have varying number of cell images ranging from 10 to 90. In total we have 3691 cell images from 105 cases. All cases originated from the archives of either City of Hope National Medical Center in California, University of Pennsylvania of School of Medicine, Spectrum Health System, Grand Rapids, MI or Robert Wood Johnson University Hospital at the University of Medicine & Density of New Jersey.

(a) RWJ   **(b)** PEN   **(c)** CAL   **(d)** SHS
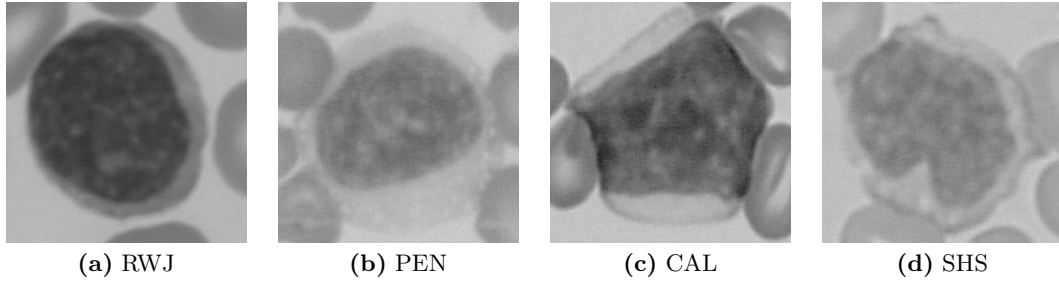
Fig. 6 Mantle Cell Lymphoma (MCL) samples from four different institutions. (a) Robert Wood Johnson University Hospital. (b) University of Pennsylvania of School of Medicine. (c) City of Hope National Medical Center in California. (d) Spectrum Health System, Grand Rapids, MI. The images reflect the obvious variations in imaging conditions among different institutions.

There were obvious variations in the staining characteristics of specimens among the institutions, which were introduced because of differences in manufacturers of the dyes, choices in automated stainers and due to the overall intensity variations. All of these variables led to variations in shadowing, shading, contrasts and highlighting cues providing an added challenge for the classification algorithms. Four MCL samples from different institutions are shown in Figure 6, which demonstrates the imaging variations among different institutions.

Stained specimens were examined by a certified hematopathologist using an Olympus AX70 microscope equipped with a Prior 6-way robotic stage and motorized turret to locate, digitize and store specimens. The system utilizes interactive software developed in Java and C++. The imaging components of the system consist of an Intel-based workstation interfaced to an Olympus DP70 color camera featuring 12-bit color depth for each color channel and 1.45 million pixel effective resolution. Figure 7 shows samples from normal and each disorder category originated from Robert Wood Johnson hospital. As seen in the images our cell database covers a wide range of characteristics for each disease category.

5.2 Test Methodology

The texture statistics of the cell images from a single case are similar to each other. As a result, the division of test and training sets without obeying the separation of cells based on per case (patient), produce biased results towards better classification rates.

We perform *leave one out* tests in our experiments. We select all the cell images from a single case as the test set and the remaining cell images in the database as the training set. The cells from the selected case are classified using the trained classifier. Training is repeated for each case (patient). In Section 5.6, we also present results for 10-fold cross validation, where a model can be trained using some cells of a case and used to classify some other cells of the same case. We refer to this scheme as not obeying the separation.

We present the results for two different tests: cell classification and case classification. In cell classification, we predict the label of each cell with the trained classifier. In the case classification, we assign the label of the case according to the majority voting among its cells. Notice that there are variable number of cell images per case, ranging from 10 to 90.

(a) Benign

(b) CLL

(c) MCL

(d) FCC

(e) Acute Leukemia

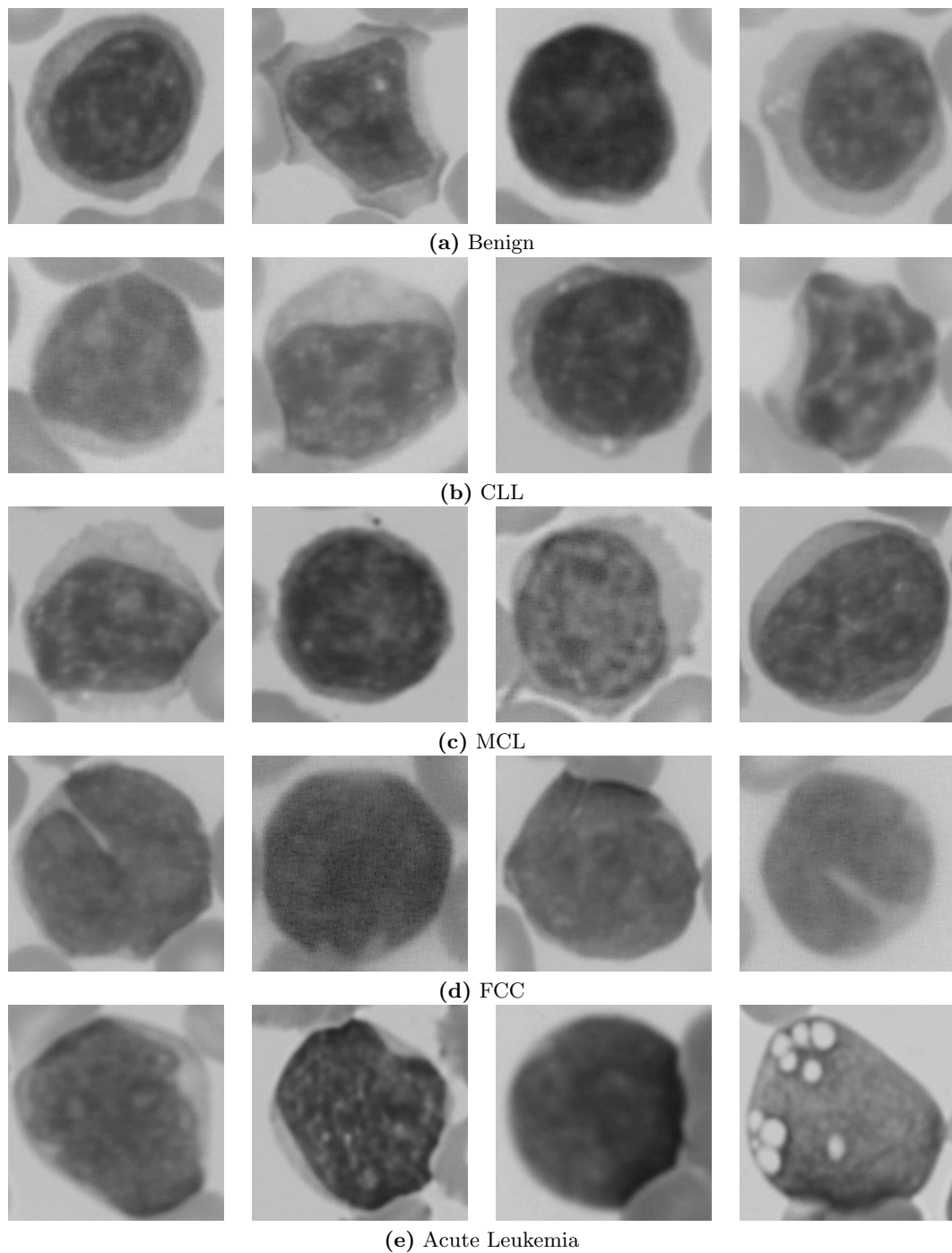**Fig. 7** Samples from normal and each disorder category from Robert Wood Johnson (RWJ) University Hospital. Even from a single institution, the samples show great variability.

5.3 Filter Banks

In the *first experiment*, we compare the texture features generated by using **M8** filter bank with **LM** [30], **S** [39], **M4** [44] filter banks and the local neighborhood method [45]. The **LM** filter bank consists of 48

	M8	S	LM	M4	Local Neigh.
Cell classification	**84.45**	84.04	82.64	78.98	75.62
Case classification	**89.52**	90.48	90.48	84.76	82.86

Table 1 Comparison of **M8** filter bank with features constructed by different filter banks and local neighborhood method. The results are ordered according to cell classification rates.

anisotropic and isotropic filter: first and second derivative of Gaussians at 6 orientations and 3 scales; 8 Laplacian of Gaussian filters and 4 Gaussian filters. The **S** filter bank consists of 13 rotationally symmetric filters and **M4** filter bank is similar to **M8** filter bank except, edge and bar filters appear only at single scale.

Initially, $n_s = 30$ random cell images are selected from each of the five classes, and the images are convolved with the filter banks. Also, the local neighborhood based features are constructed by stacking 7×7 neighborhood of each pixel. We do *not* normalize the images while constructing local neighborhood based features since the method uses local intensity information.

For nuclear texture we use $k_m = 30$ cluster centers, and for the cytoplasm texture $k_m = 15$ cluster centers, from each class. Therefore, the texton library has 150 textons for nuclei and 75 textons for the cytoplasms, total of 225 bin histogram for each cell.

The classification performance of different features are given in Table 1. The results indicate that **M8**, **S** and **LM** outperforms the **M4** filter bank and local neighborhood method. There are not obvious differences among the **M8**, **S** and **LM** filter banks. The case classification performance of **LM** and **S** filter banks are slightly better than **M8** whereas cell classification performances support the inverse argument. We consider cell classification performance as more important, since cases are classified according the majority voting of the cells and a few classified/misclassified samples among a case can drastically change the result. Moreover, **M8** filter bank is the most compact space which has 8 features whereas **LM** and **S** filter banks have 48 and 13 features, respectively. The clustering and quantization steps take much longer time using the later methods, e.g., one hour for **M8** vs. eight hours for **LM**.

5.4 Classification Methods

In the *second experiment* we compare the one-against-one SVMs with three classification algorithms: Logit-Boost, one-against-all SVMs, kNN.

Nearest neighbor classifier with the χ^2 distance metric is the widely applied classification algorithm used with histogram based texture representation. In kNN classification [19, p.415], the closest k_n training samples to the query point are detected and the query point is labeled with the class having the majority votes among the detected points. It is shown with the experiments that among the other possible choices for the distance function (KL-divergence, Bhattacharya distance, Euclidean distance), χ^2 distance performs best for the texture similarity measure. The χ^2 distance between two one-dimensional histograms h_1 and h_2 is measured as

$$\chi^2(h_1, h_2) = \frac{1}{2} \sum_{t=1}^{p} \frac{(h_1(t) - h_2(t))^2}{h_1(t) + h_2(t)}. \tag{5}$$

We select the optimum value of the number of neighbors parameter as $k_n = 15$, via cross-validation. Since χ^2 distance measures dissimilarity between two distributions we do *not* normalize each feature to have zero mean standard deviation for kNN classification, where as we perform normalization for other methods.

The second method, for comparison is multiclass LogitBoost classifier [13]. LogitBoost algorithm learns an additive multiple logistic regression model by minimizing negative log likelihood with quasi-Newton

iterations. The probability of a sample $\mathbf{x}$ being in class l is given by

$$p_l(\mathbf{x}) = \frac{e^{F_l(\mathbf{x})}}{\sum_{j=1}^{c} e^{F_j(\mathbf{x})}} \qquad \sum_{j=1}^{c} F_j(\mathbf{x}) = 0 \tag{6}$$

where $F_l(\mathbf{x})$ is an additive function

$$F_l(\mathbf{x}) = \sum_{m=1}^{M} f_{ml}(\mathbf{x}). \tag{7}$$

At each boosting iteration m, the algorithm learns the weak classifiers $f_{mj}(\mathbf{x}), j = 1...c$ by fitting weighted least squares regressions of training points $\mathbf{x}_i, i = 1...n$ to response values z_{ij} with weights w_{ij} where

$$z_{ij} = \frac{y_{ij}^* - p_j(\mathbf{x}_i)}{p_j(\mathbf{x}_i)(1 - p_j(\mathbf{x}_i))} \qquad w_{ij} = p_j(\mathbf{x}_i)(1 - p_j(\mathbf{x}_i)) \tag{8}$$

and y_{ij}^* is the binary class indicator such that $y_{ij}^* = 1$ if class of $i-th$ sample $y_i = j$, and 0 otherwise.

We utilize *regression stumps* as weak learners, which are regression trees with a single split

$$f(\mathbf{x}) = \begin{cases} a \text{ if } \mathbf{x}^t < \theta \\ b \text{ else.} \end{cases} \tag{9}$$

We learn the regression coefficients a, b, the threshold θ while $\mathbf{x}^t$ denotes the $t-th$ dimension among the 225 dimensions of the feature vector $\mathbf{x}$. In our implementation we performed $M = 300$ boosting iterations. We refer readers to [13] for more technical details.

For SVM classifiers we use linear kernel and a soft penalty ($\gamma = 0.01$) for training errors [26, Chapter 11]. The classification rates are given in Table 2. Results indicate that we achieve major improvements over the widely used kNN based texture classifier with the introduction of SVMs or LogitBoost. The one-against-one SVM and LogitBoost classifiers produced comparable results, while outperforming the other methods significantly. The performance of one-against-one SVM classifier is better than LogitBoost classifier in cell classification. However, LogitBoost has certain advantages over SVM. In medical applications, it is also important to report the uncertainty about an estimation. Since LogitBoost classifier estimates the posterior distribution of class labels through (6), with this method we can describe the uncertainty of the estimation for each individual cell. In our application, we utilize one-against-one SVM classifier since it produces most accurate results.

We achieve very successful results since even the most experienced doctors can predict the correct label after investigating several other medical records besides images. In a similar setup, but including fewer cases from normal and three lymphoproliferatie disorders (four class problem), three different human experts could only classify less than 70% of the cells correctly [5], which illustrates the superior performance of our approach.

In Table 3 and Table 4 we present the confusion matrices for cell and case classification using one-against-one SVM. The rows of the table show the actual cell classes and the columns show the predicted cell classes. The normal and acute cells are classified accurately, whereas there is some confusion among CLL, MCL and FCC cells. In the case classification almost all of the classes are predicted correctly, and only FCC cases have several misclassifications. This is mainly because we have limited number of training examples from the FCC cases.

Besides five class classification problem, we diagnosed the cells and the cases as normal vs. disorder. Since the problem is binary classification, one-against-one and one-against-all SVMs reduced to binary SVM classifier. The classification rates both for cells and cases are given in Table 5. The results indicate that we can diagnose a case as being normal or disorder almost perfectly, only a single case is misclassified among the whole database.

	One-Ag.-One SVM	LogitBoost	One-Ag.-All SVM	kNN
Cell classification	**84.45**	83.14	81.60	81.17
Case classification	**89.52**	89.52	87.62	84.76

Table 2 Cell and case classification rates of different classification algorithms.

	Normal	CLL	MCL	FCC	Acute Leukemia
Normal	**734**	64	11	1	0
CLL	35	**504**	49	63	0
MCL	11	78	**375**	27	67
FCC	14	62	31	**132**	2
Acute Leukemia	0	0	59	0	**1372**

Table 3 Confusion matrix of cell classification for one-against-one SVM.

	Normal	CLL	MCL	FCC	Acute Leukemia
Normal	**19**	0	0	0	0
CLL	0	**18**	1	1	0
MCL	0	2	**14**	0	2
FCC	2	1	1	**5**	0
Acute Leukemia	0	0	1	0	**38**

Table 4 Confusion matrix of case classification for one-against-one SVM.

	SVM	LogitBoost	kNN
Cell classification	**98.09**	97.13	96.29
Case classification	**99.05**	99.05	99.05

Table 5 Normal vs. disorder classification rates.

5.5 Other Features

In the *third experiment* we compared the texture based representation with several other features that are commonly used for hematopathology diagnoses. The first set of features are related to area of the cell. We use nucleus and cytoplasm area and nucleus/cytoplasm area ratio.

The second set of features are related to the shape of the nucleus. We analyze the shape of the nucleus based on elliptic Fourier descriptors [27] which are made invariant to changes in location, orientation and scale [5]. We achieve rotation invariance by compensating for the arbitrary position of the starting point on the contour and for the arbitrary orientation of the contour. Scale invariance is achieved by normalizing each Fourier coefficient. The following conditions are considered.

- If the first harmonic locus is an ellipse, the rotation is defined relative to the semi-major axis of the locus and we normalize the coefficients by the magnitude of the semi-major axis.
- If the first harmonic locus is circular, the rotation is made with respect to the line defined by the centroid of the contour and the most distant point on the contour and we normalize the coefficients by magnitude of the radius.

We obtain translational invariance by removing the DC coefficient from the Fourier series. We retrieve 16 harmonics (64 coefficients) for the shape of each nucleus.

We present the *one-against-one* SVM classification results for each of the features and the combination of all the features in Table 6. For the combined features we stack all the features into an array. We see

	Shape	Area	Texture	Combined
Cell classification	47.43	66.96	84.45	84.62
Case classification	50.47	70.48	89.52	91.42

Table 6 Classification rates, based on area, shape, texture and combined features utilizing one-against-one SVMs.

	Normal	CLL	MCL	FCC	Acute Leukemia
Normal	**19**	0	0	0	0
CLL	0	**18**	1	1	0
MCL	0	2	**14**	0	2
FCC	1	0	1	**7**	0
Acute Leukemia	0	0	1	0	**38**

Table 7 Confusion matrix of case classification using combined features utilizing one-against-one SVMs.

that neither area based nor shape based features are alone enough to perform classification. The texture based features outperform both of the other features significantly. Notice that, although indirectly, the area information is presented inside the texture features, since each bin of the texton histogram is equal to the number of occurrence of the texton in the image. There are minor improvements from texture based representation, 84.45%, to combined features, 84.62%, in cell classification and 89.52% to 91.42% in case classification.

The distribution of the classification performances according to different disorders show variation from texture based features to combined features. The confusion matrix of case classification using combined features are given in Table 7. Usually in the advanced stages of FCC the nuclei show variability from the other diseases. We see that two more FCC cases are correctly classified with combined features relative to Table 4. The results almost did not affect the other classes which supports the claim. We achieve only minor improvements over the texture features with the introduction of morphological features such as area and shape.

5.6 Comparison with Previous Method

In this section we compare our approach with the method of [5]. The problem considered in [5] is a subset of our problem, where only four classes are considered (Benign, MCL, FCC, CLL). The cell database of [5] contains only 261 specimens and the testing is performed by adopting 10-fold cross validations which do not obey separation based on patient.

The results of [5] is given in Table 8. To directly compare our results with [5] and illustrate the effect of test methodology, we also performed 10-fold cross validations and presented the cell classification results in Table 9. Even though the problem that we solve is more difficult (one more class), we see that our results are significantly better than [5] except for FCC class. Only the classification of FCC cells were slightly better in [5], but we note that there were only 20 FCC cells in their experiments.

The classification rates of our method with 10-fold cross validation tests are significantly higher than the leave-one-out tests performed previously. The cell classification rate changed from 84.45% to 93.18%. We see that the separation of training and test sets without obeying case separation, produces biased results towards better performances. The specimens from a single case may have similarities to each other, which are uncorrelated to the class of the disorder.

	Normal	CLL	MCL	FCC	No Decision
Normal	**73.0**	13.4	0.0	12.0	1.6
CLL	7.0	**83.9**	7.1	2.0	0
MCL	0	13.6	**83.3**	1.4	1.7
FCC	5.0	2.5	0.0	**90.0**	2.5

Table 8 Confusion matrix of cell classification rates of [5].

	Normal	CLL	MCL	FCC	AML
Normal	**96.2**	3.4	0.4	0.0	0.0
CLL	2.9	**90.4**	3.9	2.8	0
MCL	1.5	6.0	**83.6**	1.5	7.4
FCC	1.9	9.7	6.2	**81.4**	0.8
AML	0.0	0.0	1.4	0.0	**98.9**

Table 9 Confusion matrix of cell classification rates using 10-fold cross validation utilizing one-against-one SVMs.

6 Discussion

In many areas of pathology, the intrinsic variability in diagnostic complexity is compounded by a continuing lack of standard criteria for the identification of diseases and their histologic features. In the case of some lymphoproliferative disorders, most pathologists have the opportunity to review such a limited number of cases. There exists a striking disparity between the diagnoses of an expert in hematopathology and the pathologists in community hospitals. Using advanced imaging and computational tools might potentially enable investigators to detect and track subtle changes in measurable parameters.

As part of our ongoing PathMiner project, we have already described the design, development, and evaluation of an Image Guided Decision Support system for unsupervised imaging, analysis, and archiving of hemapathology specimens [4,5,49]. In our studies, nuclear texture was shown to be the most important discriminating feature for discriminating among a set of malignant lymphomas and leukemia which can sometimes be confused with one another during routine microscopic evaluation [12]. In the current paper we have investigated the statistical optimization of the underlying algorithms. Our experiments focused on the utilization of SVMs. Even with the inherent difficulties in differentiating among the disorders under study, classification results throughout our studies using texton histogram representation showed performance improvement through introduction of new classifiers. We achieve very successful results considering the difficulty of the problem.

The literature ascribes much of the difficulty in rendering consistent evaluation of expression patterns in cancer tissue microarrays to subjective impressions. When characterizations are based upon computer-aided analysis, objectivity reproducibility and sensitivity improve considerably. Encouraged by the results generated during the course of our studies we plan to explore the use of texture information for discriminating between healthy and cancerous tissues in immunofluorescing pathology specimens including cancer tissue microarrays.

7 Originality and Contribution

This study describes a texture based solution which distinguishes between normal cells and four different hematologic malignancies. A new representation for cell images is introduced utilizing texture features. The texton libraries for cytoplasmic and nuclear components of the cell images are constructed and images are represented with two histograms corresponding to both regions.

Utilizing SVMs with the proposed representation, significant classification improvements are observed over the existing texture classification techniques. It is also shown that using multiclass LogitBoost algorithm, it is possible to infer about the uncertainty of the estimation without decreasing the performance significantly.

Experiments are conducted on a cell database consisting of samples from four different hospitals, 105 cases and 3691 cell images. The database covers wide range of characteristics for each disorder class and includes obvious variations in the imaging conditions among different institutions. Detailed experiments are reported comparing the proposed approach with the selection of other features and classification techniques that are commonly used in hematopathological diagnosis, and the existing methods on the similar problems.

Acknowledgements

References

1. A. Aisenberg, "Coherent view of non-Hodgkin's lymphoma.," *J. Clin. Oncol.*, vol. 13, pp. 2656–2675, 1995.
2. F. Chabat, G. Yang, and D. Hansell, "Obstructive lung diseases: texture classification for differentiation at ct," *Radiology*, vol. 228, pp. 871–877, 2003.
3. J. Chan, P. Banks, M. Cleary, G. Delsol, C. De Wolf-Peeters, B. Falini, K. Gatter, T. Grogan, N. Harris, and P. Isaacson, "A revised European-American classification of lymphoid neoplasms proposed by the International Lymphoma study group - A summary version.," *Am. J. Clin. Pathol.*, vol. 103, pp. 543–560, 1995.
4. W. Chen, P. Meer, B. Georgescu, W. He, L. A. Goodell, and D. Foran, "Image mining for investigative pathology using optimized feature extraction and data fusion.," *Computer Methods and Programs in Biomedicine*, vol. 79, pp. 59–72, 2005.
5. D. Comaniciu, P. Meer, and D. Foran, "Image-guided decision support system for pathology," *Machine Vision and Applications*, vol. 11, pp. 213–224, 1999.
6. C. Cortes and V. Vapnik, "Support vector networks," *Machine Learning*, vol. 20, pp. 273–297, 1995.
7. R. Cotran, V. Kumar, T. Collins, and S. Robbins, *Pathologic Basis of Disease*. W.B. Saunders Company, fifth edition, 1994.
8. N. Cristianini and J. Shawe-Taylor, *Support Vector Machines and Other Kernel-Based Learning Methods*. Cambridge University Press, 2000.
9. O. Cula and K. Dana, "3D texture recognition using bidirectional feature histograms," *Intl. J. of Computer Vision*, vol. 59, no. 1, 2004.
10. R. Duda, P. Hart, and D. Stork, *Pattern Classification*. Wiley, second edition, 2001.
11. A. Efros and T. Leung, "Texture synthesis by non-parametric sampling," in *Proc. 7th Intl. Conf. on Computer Vision,* Kerkyra, Greece, September 1999, pp. 1033–1038.
12. D. Foran, D. Comaniciu, P. Meer, and L. Goodell, "Computer-assisted discrimination among lymphomas and leukemia using imunophenotyping, intelligent image repositories and telemicroscopy.," *IEEE Trans. on Infor. Tech. in Biomedicine*, vol. 4, pp. 265–273, 2000.
13. J. Friedman, T. Hastie, and R. Tibshirani, "Additive logistic regression: A statistical view of boosting," *Ann. Statist.*, vol. 28, no. 2, pp. 337–407, 2000.
14. R. Galloway, "Texture analysis using gray level run lengths," *Comput. Graphic. Image Processing*, vol. 4, pp. 172–179, 1975.

15. J. Garcia-Conde and F. Cabanillas, "Cell lymphoma: A lymphoproliferatie disorder associated with aberrant function of the cell cycle.," *Leukemia*, vol. 10, pp. 78–83, 1996.

16. R. Haralick, "Statistical and structural approaches to texture," *IEEE*, vol. 67, pp. 786–804, 1979.

17. R. Haralick, K. Shanmugam, and I. Dinstein, "Textural features for image classification," *IEEE Trans. Syst. Man Cybern.*, vol. 3, pp. 610–621, 1973.

18. K. Hassan, T. Tweed, and S. Miguet, "A multi-resolution approach for content-based image retrieval on the grid–application to breast cancer detection," *Methods of information in medicine*, vol. 44, pp. 211–214, 2005.

19. T. Hastie, R. Tibshirani, and J. Freidman, *The Elements of Statistical Learning.* Springer, 2001.

20. D. Heeger and J. Bergen, "Pyramid-based texture analysis/synthesis," in *SIGGRAPH '95: Proc. of the 22nd Annual Conf. on Computer Graphics and Interactive Techniques*, 1995, pp. 229–238.

21. A. Hertzmann, C. Jacobs, N. Oliver, C. B., and D. Salesin, "Image analogies," in *SIGGRAPH '01: Proc. of the 28th Annual Conf. on Computer Graphics and Interactive Techniques*, 2001, pp. 327–340.

22. C. Hsu and C. Lin, "A comparison of methods for multiclass support vector machines," *IEEE Transactions on Neural Networks*, vol. 13, pp. 415–425, 2002.

23. Y. Huang, J. Chen, and S. W.C., "Diagnosis of hepatic tumors with texture analysis in nonenhanced computed tomography images," *Academic radiology*, vol. 13, pp. 713–720, 2006.

24. T. Ikeda and M. Hagiwara, "Content-based image retrieval system using neural networks," *Intl. J. of Neural Systems*, vol. 10, pp. 417–424, 2000.

25. M. Jaulent, C. Le Bozec, Y. Cao, E. Zapletal, and P. Degoulet, "A property concept frame representation for flexible image-content retrieval in histopathology databases," in *AMIA Symp.*, 2000, pp. 379–383.

26. T. Joachims, *Making Large-Scale SVM Learning Practical. Advances in Kernel Methods - Support Vector Learning.* MIT-Press, 1999.

27. F. Kuhn and C. Giardina, "Elliptic Fourier features of a closed contour," *Computer Graphics Image Processing*, vol. 18, pp. 236–258, 1982.

28. C. Le Bozec, E. Zapletal, M. Jaulent, H. D., and P. Degoulet, "Towards content-based image retrieval in a his-integrated pacs," in *AMIA Symp.*, 2000, pp. 477–481.

29. T. Lehmann, B. Wein, J. Dahmen, J. Bredno, F. Vogelsang, and M. Kohnen, "Content-based image retrieval in medical applications: A novel multistep approach," in *Proceedings of SPIE: Storage and Retrieval for Media Databases 2000*, volume 3972, 2000, pp. 312–320.

30. T. Leung and J. Malik, "Recognizing surfaces using three-dimensional textons," in *Proc. 7th Intl. Conf. on Computer Vision,* Kerkyra, Greece, 1999, pp. 1010–1017.

31. J. Mao and A. Jain, "Texture classification and segmentation using multiresolution simultaneous autoregressive models," *Pattern Recognition*, vol. 25, pp. 173–188, 1992.

32. M. Mavroforakis, H. Georgiou, N. Dimitropoulos, D. Cavouras, and S. Theodoridis, "Mammographic masses characterization based on localized texture and dataset fractal analysis using linear, neural and support vector machine classifiers," *Artif. Intell. Med.*, vol. 37, pp. 145–162, 2006.

33. N. Mudigonda, R. Rangayyan, and J. Desautels, "Gradient and texture analysis for the classification of mammographic masses," *IEEE Trans. Med. Imaging*, vol. 19, pp. 1032–1043, 2000.

34. B. Nielsen, F. Albregtsen, and H. Danielsen, "Prognostic value of adaptive textural features–the effect of standardizing nuclear first-order gray level statistics and mixing information from nuclei having different area," *IEEE Trans. Medical Imaging*, vol. 23, pp. 73–84, 2004.

35. B. Nielsen and H. Danielsen, "Prognostic value of adaptive textural features–the effect of standardizing nuclear first-order gray level statistics and mixing information from nuclei having different area," *Cellular oncology*, vol. 28, pp. 85–95, 2006.

36. L. Rajesh, S. Pattari, G. G., P. Dey, and R. Srinivasan, "Image morphometry of acute leukemias. comparison between lymphoid and myeloid subtypes.," *Anal. Quant. Cytol. Histol.*, vol. 26, pp. 57–60, 2004.

37. I. Ricketts, H. Banda-Gamboa, A. Cairns, and K. Hussein, "Automatic classification of cervical cells-using the frequency domain," in *IEE Coll. on App. of Im. Proc. in Mass Health Screening*, volume 9, 1992, pp. 1–4.

38. C. Rozman and E. Montserrat, "Chronic lymphocytic leukemia.," *The New England Journal of Medicine*, vol. 333, pp. 1052–1057, 1995.

39. C. Schmid, "Constructing models for content-based image retreival," in *Proc. IEEE Conf. on Computer Vision and Pattern Recognition,* Kauai Marriott, Hawaii, 2001, pp. 39–45.

40. K. Schmid, N. Angerstein, S. Geleff, and A. Gschwendtner, "Quantitative nuclear texture features analysis confirms who classification 2004 for lung carcinomas," *Modern Pathology*, vol. 19, pp. 453–459, 2006.

41. F. Schnorrenberg, C. Pattichis, C. Schizas, and K. Kyriacou, "Content-based retrieval of breast cancer biopsy slides," *Technology and Health Care*, vol. 8, pp. 291 – 297, 200.

42. H. Sheshadri and A. Kandaswamy, "Experimental investigation on breast tissue classification based on statistical feature extraction of mammograms," *Comput. Med. Imaging Graph.*, vol. 31, pp. 46–48, 2007.

43. G. Vadlamudi, "Leukemic phase of mantle cell lymphoma: Two case reports and review of the literature.," *Arch. Pathol. Lab. Med.*, vol. 120, pp. 35–40, 1996.

44. M. Varma and A. Zisserman, "Statistical approaches to material classification," in *Proc. 7th. European Conf. on Computer Vision,* Copehagen, Denmark, 2002.

45. M. Varma and A. Zisserman, "Texture classification: Are filter banks necessary?," in *Proc. 9th Intl. Conf. on Computer Vision,* Nice, France, volume 2, June 2003, pp. 691–698.

46. R. Walker and P. Jackway, "Statistical geometric features-extensions for cytological texture analysis," in *Proc. 13th Intl. Conf. on Pattern Recognition*, volume 2, 1996, pp. 790–794.

47. G. Wyszecki and W. Stiles, *Concepts and Methods, Quantitative Data and Formulae.* Wiley, New York, 1982.

48. C. Xu and J. Prince, "Snakes, shapes, and gradient vector flow," *IEEE Trans. on Image Processing*, vol. 7, no. 3, pp. 359–369, 1998.

49. L. Yang, P. Meer, and D. Foran, "Unsupervised segmentation based on robust estimation and color active contour models," *IEEE Trans. on Information Technology in Biomedicine*, vol. 9, pp. 475–486, 2005.